FORTE Measurements of Global Optical Lightning Waveforms and Implications for Optical Lightning Detection

Michael Peterson[1]

[1]ISR-2, Los Alamos National Laboratory, Los Alamos, New Mexico

Corresponding author: Michael Peterson (mpeterson@lanl.gov), B241, P.O. Box 1663 Los Alamos, NM, 87545

Key Points:

- Variations in optical emission and scattering in the surrounding clouds create a diverse collection of optical lightning waveforms
- Large-footprint sensors such as the FORTE PDD detect broad / dim emissions because all pulse energy contributes to detection
- Increasing the spatial or temporal resolution of pixelated instruments offers greater pulse detail at the cost of missing broad / dim events
-

Abstract

Lightning processes generate a diverse collection of optical pulses depending on how current traverses the lightning channels. These signals are then broadened spatially and temporally via multiple scattering in the clouds. The resulting optical waveforms measured from space with instruments like the photodiode detector (PDD) on the Fast On-orbit Recording of Transient Events (FORTE) satellite have a variety of shapes. In this study, we use coincident optical and Radio Frequency (RF) measurements to document the properties of optical PDD waveforms associated with different types of lightning, estimate delays from scattering in the clouds, and comment on how pulse shape impacts optical lightning detection.

We find that the attributes of optical pulses recorded by the PDD are generally consistent with prior studies, but vary across the globe and with event amplitude. The brightest lightning tends to be single-peaked with faster rise times (median: ~100 µs) and shorter effective widths (median: ~400 µs). Dim events also include cases of broad optical waveforms with sustained optical emission throughout the PDD record, which the pixelated FORTE LLS instrument has difficulty detecting. We propose that this is due to the optical signal being divided between individual pixels that are each, individually, not bright enough to trigger the LLS. We use PDD waveforms and Monte Carlo radiative transfer modeling to demonstrate that increasing the temporal and spatial resolution of a pixelated lightning imager will make it more difficult to detect these broad / dim pulses as their energy becomes divided between additional pixels / integration frames.

Plain Language Summary

Lightning generates pulses of light following the extreme heating produced by its electrical currents. These emissions must then transmit through the cloud to reach the lightning sensors on satellites. Variations in current and the severity of scattering lead to many different types of optical lightning waveforms being recorded from orbit. We use FORTE measurements to document the different types of optical waveforms that can result from lightning. Our global results generally agree with prior studies with more limited samples. However, we also find that these pulse characteristics vary across the globe and with the intensity and origin of the light source. These variations stem from physical differences in the flash, the amount of scattering that occurs within the clouds, and the ability of the sensor to detect a pulse of a given shape – with pixelated sensors less able to resolve faint and broad lightning emissions than wide-FOV instruments.

1 Introduction

Lightning phenomena such as strokes generate broadband emissions throughout the optical and Radio-Frequency (RF) portions of the electromagnetic spectrum (e.g., Salanave, 1961, 1964; Christian and Goodman, 1987; Cummins et al., 2009). Even when these emissions occur at precisely the same time, they experience different propagation effects when traveling from the source to a space-based instrument. RF emissions in the Very High Frequency (VHF) band primarily interact with the ionosphere, which introduces a frequency-dependent delay in the signals as they transmit to space. The severity of this "chirp" depends on the Total Electron Content (TEC) of the ionosphere along the path taken by the signals, and mathematical models have been developed to correct the wideband VHF signals recorded by FORTE to their Vacuum Time of Arrival (VTOA) while also retrieving ionospheric parameters (Massey et al., 1998; Jacobson et al., 2000; Roussel-Dupré et al., 2001).

The optical emissions from lightning, meanwhile, are primarily modified during radiative transfer through the cloud medium surrounding the source (Thomson and Krider, 1982). Multiple scattering within the clouds directs the optical photons along different paths to the satellite. If the emitter were a perfectly-impulsive point source, then scattering in a planar homogeneous cloud would broaden the spatial radiance distribution at the cloud top from a point source into a Gaussian pulse with a finite width (Light et al., 2001a). More realistic clouds with complex shapes (Peterson, 2020) and compositions (Brunner and Bitzer, 2020) can cause the pulses to be finite but not, necessarily, Gaussian. In either case, the different path lengths experienced by these photons before reaching the cloud-top cause different photons to arrive at different times, thereby broadening the waveform temporally from an impulsive event into a pulse with a finite duration (Koshak et al., 1994; Suszcynsky et al., 2000; Light et al., 2001b).

The combination of variations in how electrical currents traverse the lightning channels and the broadening effects of scattering cause optical lightning pulses to produce a diverse collection of temporal waveforms and spatial energy distributions. Prior FORTE studies with the photodiode detector (PDD) instrument

have noted that different types of lightning events (i.e., first return strokes, subsequent strokes, in-cloud events) tend to have different waveform amplitudes (Light et al., 2001b) and effective pulse widths (Davis et al., 2002). However, the pulse attributes associated with each type of discharge are spread over a large range, making optical classification difficult. The optical pulses recorded from orbit are subject to scattering delays from temporal broadening as well as physical delays from the RF pulse and optical pulse originating from different stages in the lightning discharges. For example, attachment to ground during a return stroke produces intense VHF emissions, but the associated optical signals at ground level can be blocked entirely by the clouds. The PDD might not trigger until the optical pulse has propagated to a high enough altitude in the cloud to be detected (above ~8-10 km from Light et al., 2002; above ~7-10 km from Thomas et al., 2000).

Suszcynsky et al. (2000) estimated the physical delays (t_{phys}) and scattering delays (t_{scatt}) in a collection of simple single-peaked PDD waveforms that could be matched to coincident RF events. They approximated t_{scatt} as the difference between the PDD pulse width and a typical value for the source pulse width from ground measurements (Mackerras, 1973; Guo and Krider, 1982). They then estimated t_{phys} by subtracting t_{scatt} from the measured correlation time (t_{corr}) between the optical and RF events. The results of this exercise were mean values for t_{corr}, t_{phys}, and t_{scatt} of 243 µs, 105 µs, and 138 µs, respectively. The reported scattering delay, while reasonable, was also smaller than the median value of 380 µs reported by Kirkland (1998). This is probably due to Kirkland (1998) including waveforms in their automated analyses that did not pass the strict manual quality controls of Suszcynsky et al. (2000).

The 138 µs mean scattering delay reported by Suszcynsky et al. (2000) equates to an additional 41 km in photon path length through the cloud compared to direct line-of-sight propagation. A portion of this increased path length is due to the spatial broadening of the optical signals that results from the photons not leaving the cloud-top at the same point. The effects of spatial broadening can be apparent in the spatial energy distributions measured from orbit with pixelated lightning imagers. In an early example, Suszcynsky et al. (2001) noted that the spatial extent of pulses mapped by the Lightning Location System (LLS) on FORTE depended on the intensity of the optical source. Brighter optical sources increase the intensity of the full scattered energy distribution, allowing cloud regions far from the source that might only receive a small fraction of the total radiant energy from the pulse to trigger the instrument.

More recently, we have been considering how the shape of the spatial energy distributions measured by lightning imagers including NASA's Lightning Imaging Sensor (LIS: Christian et al., 2000; Blakeslee et al., 2020) and NOAA's Geostationary Lightning Mapper (GLM: Goodman et al., 2013; Rudlosky et al,. 2019) depend on radiative transfer through the intervening clouds. We have documented cases of LIS and GLM "group" features (that approximate distinct optical pulses) that are extraordinarily large – even exceeding 10,000 km^2 of

simultaneously-illuminated cloud. While some of these large groups can be explained by long-horizontal optical sources, we have found that, in most cases, the active regions of the lightning channels during optical illumination are fairly compact – smaller than a nominal 64 km^2 GLM pixel. The remaining illuminated cloud area comes from radiative transfer across the surrounding cloud scene.

The appearance of LIS or GLM groups depends on the amount of cloud available for scattering along the paths photons can take to reach the satellite. Optical lightning signals are particularly intense when photons can take a relatively cloud-free path to the instrument. When optical sources occur near the cloud-top, the pulse energy is highly concentrated at a single point co-located with the source. When optical sources occur near the side of the cloud, the emissions can escape the nearby boundary and reflect off the tops or sides of neighboring clouds to reach the satellite. This is the likely origin of the "anvil superbolts" in Peterson et al. (2020) that primarily illuminate the non-raining clouds surrounding the convective core of the parent thunderstorm. The issue of normal lightning appearing to be exceptionally radiant due to these "shortcut" paths the optical signals can take to reach the satellite without significant attenuation becomes more problematic when the satellite is placed near the horizon and can directly measure sources below the overhanging anvil cloud, as modeled in Peterson (2020).

Meanwhile, optical sources that occur deep within the cloud lack these "shortcut" paths to the imager. This appears to be the case for the "stratiform superbolts" in Peterson et al. (2020) that are at least as radiant as the "anvil superbolts" despite the increased attenuation. Their optical energy becomes spread over a large area, and bright or dark anomalies can be noted in the spatial energy distribution where light can more or less easily transmit through the cloud medium. These differences in the appearance of the spatial energy distributions from optical sources near the cloud edge and sources deep within the cloud are useful for identifying cases of reflections (Peterson, 2019) and poorly-transmissive clouds (Peterson, 2021a) that might impact instrument performance and the interpretation of its data.

In this study, we consider how the shape of the optical waveform from all types of lightning events across the globe impacts optical lightning detection. We use coincident PDD and RF measurements to update the prior FORTE statistics of optical pulse properties and the estimated scattering and physical delays experienced by the optical signals for the full FORTE record. We, then, examine how the variations in pulse peak power, total energy, and pulse width impact detection between the existing PDD and LLS hardware, as well as potential future lightning imagers that are expected to have finer temporal and spatial resolutions.

2 Data and Methodology

Launched in late August, 1997, the FORTE satellite provided 12 years of het-

erogeneous global lightning data from its nearly circular orbit with a 70^{o} inclination and 825 km altitude. This data included VHF-band RF detections (1997-2003) and optical detections (1997-2010) taken under a variety of operating modes that were changed multiple times over the FORTE mission. The commanded settings differed in many ways including record length, threshold settings, which instruments were operating, and how the instrumentation was triggered (either autonomously, or cross-triggered from another FORTE sensor). The heterogenous data generated from these different modes allows FORTE to provide different perspectives on global lightning than instruments like LIS or GLM that generate a consistent view of total lightning (CG as well as IC flashes) across their observational domains. However, this can also restrict the amount of data that is available for a given analysis. The following sections will describe the individual FORTE sensors and the limitations their operating modes impose on documenting optical pulse statistics. We will also describe the National Lightning Detection Network (NLDN: Cummins et al., 2009), which we use to accurately identify the time and type of lightning events that generate PDD detections over the United States.

2.1 FORTE Optical and RF Payloads

2.1.1 The FORTE PDD

The FORTE Optical Lightning System (OLS) consisted of two instruments. The first of these, the FORTE PDD, was a silicon photodiode detector that measured broadband (0.4 m – 1.1 m) optical waveforms from transient lightning events within its 80° circular Field of View (FOV) (Kirkland et al., 2001; Suszcynsky et al., 2000). Given the 825 km altitude of the FORTE satellite, this would translate to a ground footprint of ~1200 km. PDD waveform records had a sampling interval of 15 microseconds with a variable length that was either 1.92 ms (under autonomous triggering) or 6.75 ms (under external triggering). PDD triggers were GPS time-stamped with a precision of 1 microsecond (Suszcynsky et al., 2000), permitting direct comparisons with coincident lightning measurements from similarly-precise ground-based instrumentation.

In order to mitigate false triggers from energetic particle impacts, another requirement was also imposed: the PDD waveform must exceed the background threshold for a specified number of samples. Energetic particle impacts usually result in 1-2 sample spikes in the waveform, and without this filtering a sizable fraction of PDD detections would be artifacts. The number of samples required for a trigger could be configured to between 0 and 32, and was typically set to 5 (75 microseconds). To improve consistency, we also manually omit pulses that last for < 5 samples . In addition to its autonomous mode, the PDD could also be commanded to trigger externally. Either the LLS could trigger the PDD on optically-bright events, or the FORTE VHF receivers could trigger the PDD on RF-powerful events – including events that were optically-dim (Light et al., 2002). We only consider the 1.92 ms waveforms in this study, which removes most of the external triggers.

The PDD was also subject to trigger rate limitations. The first of these limitations was a minimum intertrigger delay, which was nominally 4.4 ms (Suszcynsky et al., 2000). This means that a 1.92 ms record would be followed by 2.5 ms of dead time before the next trigger could occur. PDD triggers were also limited by a maximum trigger rate. One a certain number of triggers was reached (i.e., a multiple of 10) over a short time (often 40 ms), then the PDD would stop triggering until it received the next GPS-derived 1-Hz signal (Kirkland et al., 2001). This limitation was imposed to prevent high event rates during glint episodes from filling up the instrument data buffer, but it also caused late activity in certain flashes to be missed.

2.1.2 The FORTE Lightning Location System

The second OLS instrument was the FORTE LLS (Suszcynsky et al., 2000). The LLS was a pixelated lightning imager built from modified LIS hardware. The front-end optical assembly and Charge Coupled Device (CCD) imaging array were identical to LIS, while the operations and signal processing module was built by Sandia National Laboratories. The LLS complemented the high-speed PDD waveforms by providing geolocation information for the optical source to within the ~10 km nominal footprint size of its pixels. As with other lightning imagers, the LLS triggered autonomously whenever the total radiant energy received in one of the pixels on its 128x128 pixel imaging array during a 2.45-ms integration frame exceeded a certain threshold above the noise-riding background value. Note that there were other LLS operating modes beyond the autonomous mode (Suszcynsky et al., 2000), but since we do not use their data in this study, we do not describe them here in the interest of brevity.

LLS triggers were termed "events," but note that the meaning of this term differs between the FORTE literature and the LIS / OTD / GLM literature. LLS "events" in the FORTE literature are closer to what LIS / GLM would term "groups" or "series," as they contain one-or-more pixel detections and might have occurred in adjacent integration frames (Suszcynsky et al., 2000). By contrast, LIS / OTD / GLM would term each of these pixel detections a separate "event" (Mach et al., 2007). For consistency with modern data, we choose to adopt the LIS / GLM / OTD terminology from this point forward. When we refer to events, we mean individual pixel detections in a single integration frame. Then, groups contain all contiguous events in the same frame, series are clusters of groups in rapid succession (Peterson and Rudlosky, 2019), and flashes are clusters of groups in close spatial / temporal proximity (Mach et al., 2007).

2..1.3 The FORTE RF System

The FORTE RF system contained two different types of broadband VHF receivers connected to the two identical Log-Periodic Antennas (LPAs) mounted orthogonal to each other along FORTE's nadir-pointing boom (Jacobson et al., 1999; Suszcynsky et al., 2000; Shao and Jacobson, 2001; Light et al., 2001b). The RF system was active from late 1997 to 2003, and provided global measurements of VHF lightning events across the 26 to 300 MHz band.

The RF system could be commanded to either record from the Two And Twenty Receiver" (TATR) payload or the "HUndred Megahertz Receiver" (HUMR) payload. TATR provided VHF measurements over a 22-MHz subband from two independent receivers (TATR/A and TATR/B) that each sampled one of FORTE's LPA antennas. TATR/A and B could be tuned to measure VHF signals from different portions of the VHF spectrum, or – when synchronized to the same clock – tuned to the same frequency range to derive polarization information from transient VHF sources (Shao and Jacobson, 2001). TATR record lengths and the amount of pre-trigger / post-trigger information could also be changed on-orbit, but were typically on the order of 0.4-0.8 ms. HUMR, meanwhile, consisted of a single receiver that sampled an 85-MHz wide subband. HUMR records were generally longer then TATR records, and included the 6-ms PDD-coincident records mentioned previously. As we are exclusively considering PDD waveforms in the shorter 1.92 ms configuration, all of the FORTE RF data that we use in this study will come from TATR.

Like the PDD, the FORTE RF system had multiple triggering modes, which are summarized in Light (2020). The receivers could be commanded to trigger at a certain time to facilitate on-orbit testing, to be triggered externally by the PDD, or to trigger autonomously. The autonomous triggering relied on lightning producing transient wideband signals while terrestrial noise is typically constant on lightning time scales and concentrated at certain frequencies. To detect lightning transients, the wideband RF signal was divided into eight 1-MHz channels spaced evenly across the receiver passband. RF power was monitored in each of these channels, and an alarm was issued whenever the channel power exceeded a noise-riding threshold. Simultaneous alarms from multiple channels (usually 5) would cause the instrument to trigger and report an RF event.

TATR record lengths and the amount of pre-trigger and post-trigger data also varied over the FORTE mission. For the sake of consistency, we elect to use the most common TATR configuration that provided 0.4 ms records in this study, as it generated the greatest amount of PDD-matched data.

2.2 Coincident Detections from the National Lightning Detection Network

As with prior FORTE studies, we compare FORTE events over North America with Cloud to Ground (CG) and in-cloud events detected by NLDN. NLDN provides accurate location and timing information for each lightning event. It also measures the peak current of the discharge and reports whether it appears to be a CG stroke or IC event. For this study, we acquired NLDN data for the first 5 years of the FORTE mission (late 1997-2002) from Vaisala. FORTE events were matched to NLDN events by subsetting the NLDN events that were within view of the satellite, using the WGS84 ellipsoid model of the Earth to propagate the candidate NLDN events to orbit, and looking for a tight temporal coincidence with the RF and/or PDD trigger time. This is the same approach used to compute propagation delays in Suszcynsky et al. (2000).

2.3 FORTE PDD and RF Pulse Extraction and Quality Assessment

The optical and RF event records generated by the FORTE PDD and RF system generally contain one or more distinct pulses that result from various lightning processes. An example FORTE event detected by the PDD, LLS and RF system, as well as NLDN, is shown in Figure 1. The PDD (blue lines) and RF (black lines) waveforms are plotted in Figure 1a,c and e, while the LLS spatial energy distribution is shown in (b) and the radiance fall-off with distance from the brightest event is plotted in (d). This case resulted in a single TATR trigger in Figure 1a with a typical -CG waveform marked by sustained early emission, an impulsive peak upon attachment, and then falling VHF power afterwards. NLDN likewise reported a -CG associated with the strongest peak in the TATR event (blue asterisk). The PDD recorded weak cloud illumination before the stroke and increasing optical powers following attachment. The delayed PDD peak occurred 200 µs after the TATR peak and was notably broader than the VHF waveform – lasting until the end of the PDD record. At the same time, the LLS reported optical energy extending over a ~1000 km^2 area. Modeling the radiance fall-off with distance (solid line in Figure 1d) produces an estimated Half Width of Half Maximum (HWHM) in of 9 km (dashed vertical line) for this group, while the most distant event occurred 26 km away from the brightest event in the group. The optical emissions from this -CG experienced significant temporal and spatial broadening due to scattering in the clouds.

However, not all PDD and RF pulses are simple single-peaked cases where most of the energy is captured within the event record. Therefore, we must develop a method to describe the number and locations of distinct pulses and peaks within individual PDD or RF waveforms that can be used to evaluate events. We define pulses as contiguous portions of the event waveform that exceed a noise-riding background threshold, and peaks as local maxima in the waveform encompassed by a pulse. Thus, peak features are the children of pulses and pulse features are the children of events.

Pulses and peaks are identified by looping through signal amplitude from the event peak amplitude down to the noise threshold. A new pulse is declared when samples are found that (1) exceed the current level and (2) do not occur within a certain time threshold of an existing pulse. Otherwise, the existing pulse is expanded to incorporate the samples that exceed the current signal level. Different sets of amplitude and time thresholds are determined empirically for the PDD, TATR, and HUMR. The event in Figure 1 has a single PDD pulse (shaded blue in Figure 1b) and a single RF pulse (shaded blue in Figure 1c). The earlier RF peak in this case is not assigned a unique pulse because it occurred in close temporal proximity to the later peak.

We then filter PDD events based on the attributes of their pulses. Table 1 lists the numbers of PDD events including matches to LLS groups, TATR events and NLDN events. PDD events with a single optical or RF match are distinguished from all matches, and single-peaked TATR events are also distinguished. Separate counts are listed for the full PDD record (1997-2010) and the portion of the PDD record with RF (TATR / HUMR) observations (1997-2003). Note that

most but not all of the NLDN data that we have available comes from the earlier 1997-2003 period. The different PDD filters are listed in the left column and become more restrictive lower in the table. In total, we were able to match 4.3 million of the total 10.4 million PDD events to the events recorded by one of the other instruments. Most of these (4.2 million) were joint PDD / LLS detections, leaving 81,135 cases of PDD / TATR events and 55,619 PDD / NLDN events.

A particle filter is applied to remove all PDD events where the longest-lasting pulse is 75 µs. The remaining events are classified as "isolated" if no notable activity is found before the onset of the primary pulse. 43% of the PDD events that pass the particle filter (40% of matches events) are isolated waveforms. Isolated pulses might also be classified as "contained" if the end of the pulse occurs within the PDD waveform. 42% of all isolated waveforms (41% of matched events) are also contained events. Finally, the contained events that additionally have only a single peak are designated "simple" following the nomenclature of Mach et al. (2005). Most contained waveforms –78% of all events (85% of matched events) - are also simple waveforms. While only 4,179 PDD events of the 4.1 million matched events that pass the particle filter are simple cases matched with a single 1-peak TATR event and 8,092 PDD events are simple matches to NLDN strokes, both of these samples are still larger than the 237 simple cases that were considered in Suszcynsky et al. (2000). We will generally use isolated, contained, and simple PDD matches to single optical or RF events that were observed during RF record in the following sections. The filtering that use will be specified in each analysis.

3 Results

The following sections examine the attributes of PDD optical lightning waveforms and comment on how pulse shape influences lightning detection. Section 3.1 will present global statistics for general PDD events and for PDD events matched to LLS events, TATR evnts, and NLDN CG strokes. Section 3.2 then examines how pulse characteristics vary across the globe and with pulse amplitude. Section 3.3 uses the process outlined in Suszcynsky et al. (2000) to estimate physical and scattering delays for simple PDD events. Finally, Section 3.4 uses LLS and PDD observations, as well as radiative transfer modeling, to examine the effect of pulse energy being split between increasing numbers of integration frames and pixels on optical lightning detection.

3.1 PDD Optical Lightning Pulse Statistics

Many parameters have been developed to describe the shapes of optical lightning pulses. We have chosen 11 from the literature and present their mean and median values in Table 2 along with their standard deviations. All valid PDD data collected between 1997 and 2010 are considered, with specific values for contained and simple waveforms listed separately. The values of each parameter are computed for the pulse containing the event peak power. For this reason, we have distinguished the effective pulse width (computed using only the samples in the pulse feature) from the effective event width (computed using all samples in

the event waveform) – which is identical to the "effective pulse widths" reported in prior studies.

The average effective event width for all valid PDD waveforms recorded between 1997 and 2010 is 706 µs, while the median is 633 µs. Kirkland (2001) reported a shorter effective event width of 592 µs, within the expected margin of error given the 407 µs standard deviation. Effective pulse widths are shorter with a mean of 633 µs and a median of 395 µs because additional pulses in complex waveforms and sustained weak emission outside of the pulse feature do not contribute to these effective widths. Considering only contained or simple waveforms also minimizes these effects. The mean effective pulse widths for contained and simple waveforms are 413 µs and 412 µs, respectively, and these values are within 15 µs (i.e., 1 PDD sample) of their corresponding effective event width values.

Full widths, rise times, and fall times are also computed with amplitude thresholds of 10%, 50% and 90%. These times correspond to the minimum amount of time before or after the peak when the signal reaches the specified threshold. If a boundary of the record is encountered before the threshold is reached, then the time from the boundary to the peak is reported. This is not an issue for contained waveforms where the signal amplitude at both the beginning and end of the waveform is required to be $< 10\%$ of the peak. The average 10-10% full width is 1091 µs for all PDD pulses and 754 µs for contained or simple pulses.

Mach et al. (2005) reported an average 10-10% full width of 677 µs for simple pulses recorded from an Unmanned AerialVehicle (UAV) flying above thunderstorms during the Altus Cumulus Electrification Study (ACES), while Goodman et al. (1988) reported an average 10-10% full width of 796 µs from all intracloud and CG discharges recorded from a NASA U-2 high-altitude aircraft. The average PDD 50-50% and 90-90% full widths of 362 µs and 95 µs for contained pulses are similarly comparable to the prior aircraft values of 345 µs and 108 µs (ACES) and 351 µs and 91 µs (U2). However, the 10-50%, 10-90% and 10-100% rise times reported by both aircraft studies are slower than the PDD contained pulses – falling between the mean values reported for contained PDD waveforms and all valid PDD events.

While the sample of contained events that the PDD recorded may be similar to the prior aircraft studies, they are not exactly the same. These PDD events were detected across the globe during all seasons of the year, while the aircraft data were limited to a number of overflights in comparably small geospatial domains. Moreover, while it is useful to focus on simple events that are most likely to correspond to distinct lightning processes, the complex waveforms from Table 1 that make up most of our sample better represent the variety of lightning events that might be captured from space.

The properties of recorded events are sensitive to the types of lightning that are detected, and will vary between these generic PDD detections and the PDD events matched with other instruments. Table 3 examines the optical pulse

characteristics of the lightning events that trigger either the LLS or TATR in addition to the PDD. Compared to the generic PDD detections, pulses that also trigger the LLS tend to be broader (mean effective event width: 763 µs compared to 706 µs) with longer rise times (mean 10-90% rise time: 378 µs compared to 336 µs) and fall times (mean 90-10% fall time: 718 µs compared to 655 µs). As the LLS triggers on total optical energy rather than peak optical power, maintaining a high signal amplitude over a longer duration is favorable for LLS detection. Meanwhile, the TATR events that result in PDD detections tend to produce optical pulses that are rather quick (mean effective event width: 571 µs) with faster rise times (mean 10-90% rise time: 255 µs) and fall times (mean 90-10% fall time: 526 µs). These differences in the characteristics of TATR-matched events are due to biases from the types of RF events that are also optically bright, leading to a PDD detection.

CG strokes produce strong optical and RF signals. Table 4 computes the optical pulse characteristics of PDD events that are matched to NLDN strokes of either negative or positive polarity. The mean effective event widths were 508 µs for -CGs and 608 µs for +CGs. Davis et al. (2002) reported mean effective event widths of 507 µs and 712 µs for PDD events matched to NLDN -CGs and +CGs. The difference in mean effective event width for +CGs is likely due to their small sample consisting of just 27 +CG matches. However, we agree with their suggestion that processes that involve extensive in-cloud activity (particularly in horizontal directions) will have broader optical pulses due to both physical reasons (i.e., currents traversing the lightning channels) and scattering delays, and this is why +CGs tend to have longer effective event / pulse widths. However, +CGs also have slower rise times in Table 4 (mean 10-90% rise time: 309 µs compared to 241 µs). This may be due to increased scattering (i..e, fewer shortcut paths for stratiform +CGs to take compared to the more common convective -CGs) or a physical delay (i.e., peak optical output might occur after the pulse reaches the cloud in -CGs, while a +CG might continue to get brighter for some time as the pulse spreads horizontally). We will consider both possibilities in Section 3.3.

3.2 Variations in PDD Optical Pulse Statistics

Because optical lightning pulse shapes vary by discharge type, we expect that the general pulse statistics presented in Tables 2 to 4 will also vary according to the types of lightning that are represented in the sample. There are many ways to subset the global sample of PDD events. For brevity, we will focus on two: the location of the events, and their peak optical power. We know that land and ocean lightning are fundamentally different. Oceanic lightning generates LIS groups that are larger and more energetic than their land-based counterparts – even when the microphysical measurements of the parent thunderstorm are otherwise similar. Additionally, oceanic lightning is more likely to exhibit lateral development than flashes over land (Peterson et al., 2016). Moreover, certain regions including the Sea of Japan, Mediterranean Sea, and Southern Ocean are known for generating powerful superbolts (Turman, 1977).

Global maps of the average PDD effective event width, 10-90% rise time, the difference between the 90-10% fall time and 10-90% rise time, and the inter-event interval are shown in Figure 2. In order to limit biases from artifacts at high latitudes where there are few lightning events, we only show cases that trigger multiple FORTE sensors simultaneously. All four parameters exhibit considerable regional differences. The greatest average effective event widths occur over the ocean where rise times are also increased, consistent with the PDD detecting a greater proportion of in-cloud pulses from these flashes. By contrast, high latitude regions over land have some of the shortest pulses, on average, with quick 10-90% rise times. Average inter-event intervals also approach the instrument view time. In other words, the PDD is more likely to detect only a single impulsive event (such as a stroke) from flashes in these regions rather than subsequent cloud illumination at different points in the flash.

These global pulse statistics are influenced by the sensitivity of the instrument. The PDD's maximum trigger rate is perhaps its greatest limitation because it biases these statistics towards early optical pulses in long-lived flashes. Most flashes that only last a fraction of a second will not be impacted, but the later emissions from flashes that develop over substantial horizontal distances and long durations (Peterson et al., 2017; Peterson, 2021b; Peterson and Stano 2021; Peterson et al., 2022a) will not be represented. Otherwise, the PDD is a capable instrument that resolves lightning emissions over multiple orders of magnitude in irradiance (Kirkland et al., 2001) including radiant strokes with high peak currents, and dim optical pulses from in-cloud processes or strokes that have been severely attenuated by scattering in the cloud medium.

To examine how pulse characteristics vary with peak optical power, Figure 3 constructs two-dimensional histograms between the peak power estimated at the source location and another event parameter. The median, 10^{th}, and 90^{th} percentile values for each peak power bin are also overlaid. Figure 3a computes the PDD effective event width statistics for each peak power using all valid PDD events. The range of effective widths for PDD events depends on peak optical power. Weak events ($< 1.5\text{x}10^9$ W) have effective widths ranging from the 75 µs minimum pulse width of the particle filter to the nearly the 1.92 ms record length. The maximum effective event widths decline as we increase in optical power, leaving only the more impulsive events.

The reason for this trend is the relative abundance of simple versus complex waveforms in each power bin. Figure 3b computes the fraction of simple PDD waveforms at each point in the 2D histogram from Figure 3a. The percentile plots, then, show the median, 10^{th}, and 90^{th} percentiles of PDD effective width for only simple PDD events. Simple events are found at all peak powers and represent a significant fraction of the events with low effective widths. Meanwhile, the broader events (i.e., > 1 ms) found only at weaker peak optical powers are predominantly complex waveforms with multiple pulses and peaks. As a result, the median PDD event widths from cases with powers $< 1.5\text{x}10^9$ W in Figure 3a slightly exceed the overall median for all pulses listed in Table 2 (633 µs), while

the median event widths for cases $> 1.5\text{x}10^9$ W are close to the median value for simple waveforms in Table 2 (407 µs). Therefore, PDD-like instrument with an equivalent threshold of $> 1.5\text{x}10^9$ W would observe an entirely different sample of optical lightning events than the PDD. Instead of detecting large numbers of complex waveforms from in-cloud activity as the flash develops over time, it would only detect the few powerful simple pulses produced by each flash during large-scale re-arrangements of charge (i.e., during strokes).

The median effective widths of these simple events do not change substantially with event peak power in Figure 3b, though the 90^{th} percentile values fluctuate over the depicted range due to changes in the underlying pulse shape statistics. The 10-90% rise time for these simple pulses (Figure 3c) decreases with increasing power while the 90-10% fall times in Figure 3d have a low-amplitude peak ($1.5\text{x}10^9$ W for the median curve) and a high-amplitude peak ($9\text{x}10^{10}$ W for the median curve) separated by a local minimum. These simple waveforms contain the complete pulse within the PDD event record and lack contributions from other pulses. Therefore, this behavior suggests that flashes in the ranges of optical power corresponding to these peaks are more likely to have additional activity following their most intense optical emission - either from sustained current flow or increased scattering delays. Furthermore, the bimodal shape of the curves implies that different populations of lightning are responsible for each peak.

The final two panels of Figure 3 test whether there is evidence for sustained lightning activity during or after these simple events. Figure 3e shows a 2D histogram of the inter-event interval after the event of interest. If the simple event occurred as part of a long-lived process (as in Figure 5 in Peterson et al., 2021), then the inter-event interval would be ~4.4 ms (bottom horizontal grey line in Figure 3e). If the next event occurred as part of a different process but still in the same flash, then the inter-event interval would occur above the bottom horizontal line and below the middle grey line at 330 ms. Finally, if the next event could not have occurred while FORTE was overhead, then the inter-event time would be above the top grey line.

The inter-event times for these simple waveforms cluster in two groups: subsequent events within the same flash, and the first pulse from a subsequent flash. Inter-event intervals tend to increase with increasing event peak power, as more powerful events become more isolated in time. Once we reach the 10^{11} W superbolt threshold, the next PDD event is just as likely to occur in a subsequent flash as it is to represent later activity in the same flash. However, $< 10\%$ of all subsequent events at all optical powers, occurred as a consecutive trigger to the event of interest. While sustained illumination over consecutive PDD triggers does occur, this long-lived illumination is not responsible for either peak in the fall time curve.

In cases where we have TATR matches, we can also compute an effective event width from the VHF waveform using the same procedure as the optical PDD data. These RF pulses are not affected by scattering in the cloud medium, but

they are also not perfect analogs to the unmodified optical source curve because the RF and optical emissions are sensitive to different aspects of the lightning discharge. Still, the effective event widths of these optical and RF waveforms are both an analog for continuous breakdowns over time. For example, +CGs have broad VHF waveforms due to the continued in-cloud development following attachment (Light et al., 2001b), and we have observed sustained constant VHF emissions over hundreds of milliseconds during widespread leader development in a FORTE megaflash (Peterson et al., 2021). We compute the RF effective event widths for TATR matches to our simple PDD events and plot a 2D histogram with PDD event peak power in Figure 3f. The effective widths of the VHF waveforms increase with increasing PDD peak optical power. Thus, the longer fall times in the higher peak from Figure 3d are at least partially explained by sustained in-cloud activity following the primary discharge.

3.3 Scattering and Physical Delays in Simple PDD Pulses

We use the approach from Suszcynsky et al. (2000) to estimate the physical delays (t_{phys}) and scattering delays (t_{scatt}) in PDD events that were matched to RF events - either TATR events or NLDN strokes. Both of these delays contribute to the total observed delay between the RF and optical pulses. This correlation time (t_{corr}) is measured as the time difference between the onset of the VHF pulse (or NLDN event time after correcting for time of flight) and the peak of the optical pulse recorded by the PDD. These points in the waveforms were chosen because they were readily identifiable and physically meaningful (Suszcynsky et al., 2000).

This approach was subject to two significant assumptions that will affect our results. The first assumption is that since VHF output is driven by changes in current (dI/dt) while optical output is riven by current (I), the VHF emissions from the source would precede the emission of the optical emissions by no longer than the rise time of the current pulse (1-10 µs) - which is small compared to typical values of t_{corr} (Suszcynsky et al., 2000). Any additional delays that we might measure would come from either the optical emissions originating from a different part of the discharge or extensive modification of the optical pulse by scattering in the clouds. The second assumption was motivated by a lack of pulse width measurements for the optical source waveform. The PDD temporal broadening measurement was defined as the difference between the optical source pulse width and the optical pulse width recorded from space. However, with the source pulse width being unknown for each PDD event, Suszcynsky et al. (2000) took a statistical approach and used a standard value of 200 µs that was derived from ground measurements of return strokes.

While the effective widths of the unmodified optical source waveforms may not be available, we do have TATR waveforms that represent the shape of the source pulse in the VHF band. While the VHF pulse may not be an ideal match for the optical pulse at the source, it could still produce a better representation of the optical source pulse width than simply assuming a single value from the literature. We will consider both approaches below.

The results of this exercise are presented in Table 5 for PDD and TATR matches, PDD and NLDN -CG Matches, and PDD and NLDN +CG matches. As with Suszcynsky et al. (2000), we only use simple single-peaked PDD events, though we rely on our automated filtering rather than a manual assessment of each PDD waveform. We also require that the TATR events be simple and single-peaked, like the PDD events. As a result, the PDD effective pulse widths are slightly different than in Table 4 with a mean of 389 µs and a median of 376 µs. If we assume the same 200 µs source pulse width as Suszcynsky et al. (2000), then the average (median) scattering delays for TATR-matched PDD events were 189 µs (176 µs), while the physical delays were 97 µs (91 µs). As it turns out, using the TATR effective pulse widths results in a very similar value for the source pulse width of 197 µs, and the resulting scattering and physical delays are essentially identical. Compared to Suszcynsky et al. (2000), the scattering delays in our sample are 51 µs greater (57 km rather than 41 km of additional path length), while the physical delays are within 8 µs of the previous values.

These TATR events include both strokes and in-cloud events. To look at strokes, specifically, we turn to the single NLDN CG matches with simple PDD events. After accounting for time of flight, we arrive at correlation times that are slightly longer than the TATR events (mean: 308 µs for -CGs, 519 µs for +CGs). This additional delay could come from either increased scattering or physical delays. The -CGs in this sample have mean effective pulse widths only 11 µs longer than the TATR events (i.e., ~50% of the correlation time difference). Therefore, when we assume a 200 µs source pulse width, the resulting scattering and physical delays are each ~10 µs longer than the TATR values. Meanwhile, NLDN +CGs generate PDD events with large correlation times and effective pulse widths. If we assume the standard 200 µs source pulse width, we arrive at particularly long scattering delays (mean: 304 µs) and physical delays (mean: 215 µs).

Comparing the delays by matched event type under the constant 200 µs source width approach, it appears that TATR events are detected earliest in the discharge and subject to the least amount of scattering modifications, which might be expected due to the contribution of in-cloud events in the TATR sample. The -CGs that are common in convective lightning then have the next-shortest delays, followed by +CGs that often occur in clouds that are relatively homogeneous and lack shortcut paths to the satellite to avoid scattering through a large optical depth of cloud. For both TATR events and NLDN +CG events, there is virtually no difference between assuming a 200 µs source pulse width or approximating the source pulse width with TATR waveforms.

However, when we apply the TATR approach to NLDN -CGs, we get a notably shorter source pulse width (mean: 178 µs), resulting in increased scattering delays (221 µs) and decreased physical delays (86 µs). The prior approach of applying the same source pulse width to all types of lightning is certainly not realistic. Suszcynsky et al. (2000) made this assumption out of a lack of source pulse width observations (particularly from sources in the clouds). The TATR effective pulse widths may not correspond to the optical pulse widths

at the source, but they probably still capture the relative differences between certain types of lightning events. Therefore, the implication of the increased scattering delays and reduced physical delays of -CG matches that the optical pulse originates from an earlier period in the discharge when the optical pulse is lower in the cloud could be valid. Verifying this would require coincident cloud-top and ground-based measurements of the same sample of lightning pulses.

In the absence of these measurements in the FORTE era, we can look for evidence of variations in scattering effects between different populations of lightning by comparing the TATR-derived scattering delays between PDD events with peak optical power. Figure 4 constructs similar 2D histograms between scattering delay and peak power, as in Figure 3. While the sample size with TATR matches is substantially reduced (particularly at higher powers), the median and 10^{th} and 90^{th} percentile curves tend towards lower scattering delays with increasing peak optical power. This suggests that the lower peak in pulse width and fall-off time curves from Figure 3 arises from narrower pulses that are subjected to increased scattering in the clouds, while the higher peak results from broad pulses that occur in clouds with somewhat reduced scattering effects.

Simultaneously broader pulses with reduced scattering at high peak powers is consistent with our observation that superbolts tend to occur in two different types of clouds. The anvil superbolts that mostly illuminate non-raining clouds surrounding the convective core are thought to be normal lightning that happens to have particularly-clear paths to the satellite, causing them to appear brighter than they otherwise would (Peterson et al., 2020). At 100 GW, these anvil superbolts comprise the majority of the superbolt sample, which could explain the low scattering delays in Figure 4. Stratiform superbolts, meanwhile, occur in homogeneous clouds that lack these shortcut paths, and should be subject to notable scattering delays. Stratiform superbolts tend to arise from intense +CG strokes (Peterson et al., 2020; Peterson and Lay, 2020; Peterson and Kirkland, 2020) that are expected to produce relatively broad source waveforms like we see in the VHF (Light et al., 2001b). While stratiform superbolts become more common with increasing peak optical power, this type of lightning should still contribute to the large spread in the scattering delay statistics in this lower range leading up to 100 GW.

3.4 The Effects of Spatial / Temporal Optical Pulse Shape on Lightning Detection

The FORTE satellite contained two optical lightning instruments: the PDD that triggered on overall peak event power, and the LLS that triggered on the total energy in one of its pixels during a 2.47 ms integration frame. The differences in how these instruments were triggered resulted in each sensor detecting a different sample of lightning. In Figure 5, we construct 2D histograms of LLS-matched PDD events and compute the LLS Detection Efficiency (DE) relative to the PDD as a function of PDD peak power and PDD total energy (Figure 5a,b) and also by PDD peak power and PDD effective event width (Figure 5c,d).

The line overlays show constant effective event widths (Figure 5a,b) and event energies (Figure 5c,d).

Since the LLS integrated the optical signals over each frame, the relative DE in Figure 5b should primarily be a function of the PDD total energy, with variations in DE at each energy largely corresponding to the varying background intensity and instrument threshold. This is generally what we see in Figure 5b, with DE values increasing from 25% to 75% between 10^5 J and 10^6 J. However, the relative LLS DE is not completely insensitive to the peak optical power of the events that result in each constant energy value. Both the most powerful pulses for a given energy in this range and the least powerful pulses have notably reduced relative DEs compared to the intermediate events. Thus, the LLS has difficulty detecting broad and dim pulses and powerful and narrow powerful pulses despite a constant total energy.

This is more easily seen in Figure 5d, which substitutes total energy for effective event width and overlays lines of constant energy. Below 2-3x10^6 J, the LLS tends to miss events that last less than 250 µs despite being primarily simple impulsive pulses (Figure 3b) such as -CG strokes (i.e., Figure 2 in Peterson and Kirkland, 2020). The missed events above 1,500 µs, meanwhile, are almost entirely complex waveforms, mostly from in-cloud processes and +CG strokes.

The integrating nature of the LLS provides two likely reasons for why these pulses are missed. The optical lightning signals recorded by the LLS are divided between different pixels according to their spatial extent and between different integration frames according to their duration and the point within the integration frame that they arrive at the satellite. Optical pulses that are particularly broad - either spatially or temporally - might have a high total optical energy, but if no individual pixel during a single integration frame receives enough energy to trigger, then the pulse will not be detected. This is expected to occur with low-altitude discharges such as strokes, where scattering causes even impulsive optical signals to be broadened, and is consistent with the increased scattering delays in Figure 4 over the same range in peak optical power. However, it is also expected to occur with the illumination of long-horizontal lightning channels in the clouds. Even before scattering effects are considered, the finite extent of the optical source ensures that the total energy emitted by the source will be divided between pixels. Moreover, the optical pulses often traverse the lightning channels over long periods of time (in the most exceptional cases we can even track their progress between subsequent LIS groups in consecutive integration frames). The resulting waveforms would be broad and complex, consistent with the PDD observations.

The questions of whether lightning is detected and how much of the flash can be resolved depend on the sensitivity of the instrument. As mentioned previously, if a PDD-like instrument had an equivalent threshold of >1.5x10^9 W, then it would rarely detect more than just the few brightest pulses in the flash, per Figure 3a. However, for lightning imagers, detection also depends on how the energy that reaches orbit is distributed in space and time. This means that

while increasing the resolution of the instrument is expected to improve the overall Signal-to-Noise ratio (SNR), it will not uniformly improve detection. Instead, it will amplify the existing biases that we see in Figure 5 towards sources with concentrated energy densities at the expense of broader pulses. Moreover, since pulse width is a function of source altitude, this will increase the detection advantage of high-altitude sources over low-altitude sources, making the instrument less capable of detecting lightning from thunderstorms where the lightning activity is concentrated near the cloud base.

To quantify the potential effects of increasing the resolution of the lightning imager on low-altitude source detection, we use the CloudScat model (Luque et al., 2020) to simulate the optical signals at 777.4 nm that leave the top of a 14-km deep essentially infinite homogeneous planar cloud from a source located at the cloud base. The background light is assumed to be negligible – either due to a nighttime background or a successful background subtraction – to examine the effects of pixel size relative to the shape of the pulse on detection with all else being equal. This scene was simulated with multiple identical pixelated instruments placed at the 825 km altitude of the FORTE satellite directly above the source that only varied by the resolution of their imaging arrays. Due to the geometry of the model setup, odd pixel counts will have the source located at the center of one of its pixels, providing an upper bounds for the radiance that could be seen from an event, while even pixel counts will have the source located at the boundaries between four adjacent pixels, providing a lower bounds radiance, as discussed in Zhang et al. (2020).

Cross sections of scene radiance from each imager are shown in Figure 6a for odd pixel resolutions and Figure 6b for even pixel resolutions. When the imager consists of a single pixel, it is essentially PDD-like, and the small size of the source compared to the enormous FOV of the pixel results in very small radiance values. Increasing the number of pixels on the imaging array improves our ability to resolve the spatial distribution of radiance across the optical pulse. This would be particularly advantageous for measuring complex energy distributions in order to infer source altitudes, identify poorly-transmissive clouds (Peterson, 2021a), and construct illuminated thundercloud imagery (Peterson, 2019).

However, the key metric for detection is the number of photons intercepted by an individual pixel, which becomes smaller as the signal is divided between increasing numbers of pixels. Figure 6c and d convert the radiances in Figure 6a,b into an effective source power as measured by each pixel. When the source is entirely contained within the pixel (i.e., for resolutions of 1 and 3 pixels in Figure 6c), the imager reports the same power of nearly 10^5 W. When the source is located at the boundaries between four pixels, as with resolutions of 2 and 4 pixels in Figure 6d, 25% of the total power is detected in each pixel. As the imager resolution increases to a finer scale than the spatial width of the optical pulse, the peak power recorded by any pixel falls drastically. If we had two instruments – one PDD-like with a resolution of 1 pixel and one LLS-like with a resolution of 128 pixels – and both had an effective threshold of $2\text{x}10^3$ W, then

this simulated pulse would be detected by the PDD-like instrument and missed by the LLS-like instrument despite the greater peak radiances that the LLS-like instrument would have measured (Figure 6a,b).

The proportion of missed lightning events relative to a PDD-like instrument only increases as we continue to increase the imager resolution beyond the 128x128 arrays used by LIS and LLS, as smaller fractions of the total optical signal from the event are used to trigger a pixel. Figure 6e computes the maximum percent of the total event power found in any pixel on the array as a function of imager pixel count up to 1024 pixels. Under ideal conditions with the light source located at the pixel center (i.e, odd counts, solid line), the brightest pixel goes from capturing all of the event power at 1 pixel to just 0.22% of the event power by 1024 pixels.

Because they can trigger on nearly all of the energy of the optical pulse, large-FOV instruments would have an advantage for detecting dim, spatially broadened optical sources against a dark background. Under daylight conditions, however, it should not be expected that the background can be entirely removed. In this case, the photons contributed by solar illumination compete with the localized signals emitted by the flash. Because SNR scales approximately with pixel area, smaller pixels would give a better overall performance during the day, despite the biases discussed previously. However, if we could combine the greater signal power fraction from larger pixels with the improved SNR performance from smaller pixels, it would allow us to resolve a larger and more diverse set of lightning pulses.

Triggering on the total local energy from all nearby pixels is one way of doing this. The dashed lines in Figure 6e report the maximum total fraction of the pulse energy in circular Regions of Interest (ROIs) of varying radii around each pixel. By summing the total energy of the 4 pixels directly adjacent to each pixel, we improve the pulse power fraction by an order of magnitude at a resolution of 1024 pixels – allowing it to operate effectively as a 300-pixel imager. Enlarging the ROI to a 3-pixel radius adds nearly another order of magnitude – bringing the fraction up to 10% of the total pulse power. Separating instrument triggering from the energies in individual pixels would allow us to trigger on a larger fraction of the optical pulse output while avoiding much of the decreased SNR from increased instrument pixel sizes.

Additionally, we also have the problem of pulse splitting between integration frames. To quantify the effects of temporal pulse splitting on detection with decreasing integration frame durations below 2 ms, we step our PDD optical waveforms from all types of lightning through a set of potential integration frames with different durations from beginning to end in 15 µs increments, compute the energy in each frame at each step, and then compute the fraction of steps that would result in a detection (i.e., the relative DE compared to the PDD) or multiple detections (i.e., the split pulse frequency) under various energy thresholds. The results of this exercise are plotted in Figure 7.

The PDD-relative DEs at each energy threshold in Figure 7a all decrease with decreasing integration frame duration, as the signal becomes divided between more frames making it less likely for one of the frames to trigger - like we saw previously with pixel resolution. Drastic reductions in DE only occur once the integration frame durations approach the effective widths of typical optical pulses, however. Shortening the integration frame durations from 2 ms to 1 ms only reduces the relative DE to ~80% (depending on the threshold), while the relative DE falls to ~50% by 500 µs. Lowering the threshold mitigates this DE loss. Almost all of the PDD events are detected with even a 500 µs integration frame at the lowest 10^5 J threshold. Zhang et al. (2020) lists a typical nighttime threshold for GLM of 423 J in the 777.4 nm band. If we assume that 4% of the broadband PDD optical energy is in this band (Suszcynsky et al., 2001), then the threshold in Figure 7 would be 1.58×10^5 J - right in this insensitive range. However, measurements taken under higher daytime thresholds would be closer to 10^6 J where the relative DE changes considerably with integration frame duration. Thus, a GLM-like instrument with a shorter integration frame - like the 1-ms Lightning Imager (LI: Grandell et al. 2014) - would be expected to have an amplified diurnal variation in performance with all else being equal. Nighttime detection would be largely unchanged, while fewer daytime pulses would be detected.

Moreover, the pulses that are detected would be more likely to trigger during multiple consecutive integration frames. Figure 7b and c plot the split pulse fractions for each combination of integration frame duration and energy threshold. Figure 7b shows the overall percentage of split pulses. Pulses are more likely to be split under lower instrument thresholds than higher instrument thresholds, as subsequent cloud illumination is usually very dim compared to the peak optical emission and not sufficient to trigger the instrument on its own when the threshold is high. However, as we move towards shorter integration frames (especially < 1 ms), the likelihood of the pulse being split between frames increases for all thresholds. To show the difference in splitting frequency that results from just shortening the integration frame, Figure 7c computes the percent difference relative to a 2-ms integration frame. Reducing the integration frame duration from 2 ms to 1 ms will only increase the frequency of split pulses by 5-10%. Further reducing it to 500 µs results in split flashes becoming 25% more common while extremely-short integration frames (100 - 200 µs) would result in split flashes being 40-50% more common.

Increasing the spatial and/or temporal resolutions of lightning imagers might improve the overall SNR or the instrument, but it is also expected to adversely affect detection of certain types of lightning pulses. This is because these instruments are designed to trigger on the amount of energy intercepted by one of its pixels during a single integration frame. We may be able to recover these missing pulses by separating instrument triggering from the resolution of the instrument, and instead trigger by summing the energies in multiple pixels and integration frames. Ideally, an approach would be developed that would allow us to trigger on a large fraction of the full emitted energy of the pulse (like the

PDD) while limiting the size of the region contributing noise but no signal.

5 Discussion and Conclusion

In this study, we use the PDD instrument on the FORTE satellite to document the characteristics of global optical lightning waveforms, to estimate the physical and scattering delays that the optical emissions were subjected to, and to comment on how waveform shape impacts lightning detection. The PDD data show that lightning generates a diverse collection of optical waveforms that range from the simple impulsive events found at all amplitudes to the persistent weak optical emission that lasts throughout the 1.92 ms PDD event record and might include multiple embedded impulsive events. Of our 10 million valid PDD events, 43% are isolated pulses that lack activity before the primary pulse, 42% of isolated pulses (18% overall) are contained pulses that cease before the end of the 1.92 ms record, and 78% of contained pulses (14% overall) are simple pulses whose waveforms have only a single peak.

The average valid PDD waveform has an effective event width of 706 µs, a 10-10% full width of 1091 µs, a 10-90% rise time of 336 µs, and a 90-10% fall time of 655 µs due to the presence of complex waveforms in the sample. If we limit our analysis to just simple waveforms, the average PDD event has an effective width of 424 µs, a 10-10% full width of 754 µs, a 10-90% rise time of 197 µs, and a 90-10% fall time of 457 µs. The shape of the waveform depends on the type of lightning discharge involved with -CG strokes being particularly quick (mean effective event widths, rise times, and fall times for simple cases of 402 µs, 180 µs, and 424 µs) and +CGs being particularly broad (mean effective event widths, rise times, and fall times for simple cases of 495 µs, 242 µs, and 439 µs). These differences appear to result from the amount of in-cloud activity during these lightning phenomena that occurs at sufficiently high altitudes in the cloud to be detected. Thus, the frequency and characteristics of observed lightning pulses depends on where lightning is occurring relative to storm structure, leading to notable regional differences across the globe.

The physical and scattering delays estimated from RF-matched simple PDD events also vary by event type. Applying the approach from Suszcynsky et al. (2000) to generic PDD and TATR matches results in an average scattering delay of 189 µs and an average physical delay of 97 µs. Average scattering delays for PDD matches to NLDN -CGs (+CGs) were 200 µs (304 µs), while average physical delays were 108 µs (215 µs). As in Suszcynsky et al. (2000), these values assume a typical value for the source pulse width of 200 µs. TATR effective event widths in the VHF band agree favorably with this value, except in the case of -CGs.

The diversity of optical pulses generated by lightning is important to consider in regards to the problem of optical lightning detection. We find that while the relative DE of LLS groups to PDD events depends primarily on total optical energy, the LLS has difficulty detecting certain particularly-narrow and particularly-broad optical pulses compared to the mid-range optical pulses with

an equal total energy. We suggest that this is due largely to the spatial extent of the optical signals. The missed narrow pulses are likely -CG strokes that might have their optical energy scattered across multiple pixels with no one pixel meeting the LLS detection threshold. Similarly, particularly-broad PDD waveforms include cases of extensive illumination of large swaths of the lightning channels that would, likewise, be divided between LLS pixels.

We use Monte Carlo radiative transfer modeling to show that increasing the spatial resolution of the lightning imager will make the detection of spatially-broad optical events more difficult. As the optical emissions from these sources become spread over a larger number of pixels, a smaller fraction of the total pulse signal is used for detection. Since most optical sources are small (Peterson et al., 2022b), the impact on instrument performance is anticipated to depend on the amount of spatial broadening in the signals from scattering in the clouds, further amplifying the existing detection advantage for high-altitude sources (that are less modified by scattering in the cloud medium) over low-altitude sources (that are severely broadened). However, if the low-altitude pulses could still be detected with a finer-resolution instrument, the greater detail in the measured spatial energy distributions would be beneficial for applications that use this product (Peterson, 2019; Peterson, 2021a; Peterson et al., 2022c-e).

Similar signal splitting also occurs between integration frames, but instrument performance is not expected to be severely degraded as long as these frames are longer than typical optical pulse widths (i.e., ~500 µs). As with the imager spatial resolution, an increased temporal resolution would resolve the light curves generated by lightning pulses in greater detail, which could be advantageous for certain applications of the lightning imager data.

A solution to all of these signal splitting effects could be to separate instrument triggering from individual pixels and integration frames in future lightning imagers. If the imager could trigger on the total energy across multiple adjacent pixels and frames, then it would be able to use most (if not all) of the energy from the lightning pulse for detection – similar to the FORTE PDD. Unlike the PDD, however, the summed data could first be filtered to prevent pixels that contain noise but no signal from contributing to the trigger. Then, returning the energies of each pixel that contributed to the event would resolve the optical pulse with an exceptional level of detail.

Acknowledgments

Los Alamos National Laboratory is operated by Triad National Security, LLC, under contract number 89233218CNA000001. Research presented in this article was supported by the Laboratory Directed Research and Development program of Los Alamos National Laboratory under project number 20200529ECR. The data presented in this study are located at Peterson (2022).

References

Blakeslee, R. J., Lang, T. J., Koshak, W. J., Buechler, D., Gatlin, P., Mach,

D. M., ... & Christian, H. (2020). Three years of the lightning imaging sensor onboard the international space station: Expanded global coverage and enhanced applications. *Journal of Geophysical Research: Atmospheres*, *125*(16), e2020JD032918.

Brunner, K. N., & Bitzer, P. M. (2020). A first look at cloud inhomogeneity and its effect on lightning optical emission. *Geophysical Research Letters*, *47*(10), e2020GL087094.

Christian, H. J., & Goodman, S. J. (1987). Optical observations of lightning from a high-altitude airplane. *Journal of Atmospheric and Oceanic Technology*, *4*(4), 701-711.

Christian, H. J., R. J. Blakeslee, S. J. Goodman, and D. M. Mach (Eds.), 2000: Algorithm Theoretical Basis Document (ATBD) for the Lightning Imaging Sensor (LIS), NASA/Marshall Space Flight Center, Alabama. (Available as http://eospso.gsfc.nasa.gov/atbd/listables.html, posted 1 Feb. 2000)

Cummins, K. L., & Murphy, M. J. (2009). An overview of lightning locating systems: History, techniques, and data uses, with an in-depth look at the US NLDN. *IEEE transactions on electromagnetic compatibility*, *51*(3), 499-518.

Goodman, S. J., Blakeslee, R. J., Koshak, W. J., Mach, D., Bailey, J., Buechler, D., ... & Stano, G. (2013). The GOES-R geostationary lightning mapper (GLM). *Atmospheric research*, *125*, 34-49.

Grandell, J., Finke, U., & Stuhlmann, R. (2009, September). The EUMETSAT meteosat third generation lightning imager (MTG-LI): Applications and product processing. In *9th EMS Annual Meeting* (pp. EMS2009-551).

Guo, C., & Krider, E. P. (1982). The optical and radiation field signatures produced by lightning return strokes. *Journal of Geophysical Research: Oceans*, *87*(C11), 8913-8922.

Jacobson, A. R., S. O. Knox, R., Franz, and D. C. Enemark, 1999: FORTE observations of lightning radio-frequency signatures: Capabilities and basic results. *Radio Sci.*, **34** (2), 337– 354, doi:10.1029/1998RS900043

Jacobson, A. R., K. L. Cummins, M. Carter, P. Klingner, D. Roussel-Dupré, and S. O. Knox, 2000: FORTE radio-frequency observations of lightning strokes detected by the National Lightning Detection Network. *J. Geophys. Res.*, **105** (D12), 15653– 15662, doi:10.1029/2000JD900103

Kirkland, M. W., D. M. Suszcynsky, R. Franz, J. L. L. Guillen, and J. L. Green (1998). Observations of terrestrial lightning at optical wavelengths by the photodiode detector on the FORTE satellite, Rep. LA-UR- 98-4098, Los Alamos Natl. Lab., Los Alamos, N.M.

Kirkland, M. W., Suszcynsky, D. M., Guillen, J. L. L., & Green, J. L. (2001). Optical observations of terrestrial lightning by the FORTE satellite photodiode

detector. *Journal of Geophysical Research: Atmospheres*, *106*(D24), 33499-33509.

Koshak, W. J., Solakiewicz, R. J., Phanord, D. D., & Blakeslee, R. J. (1994). Diffusion model for lightning radiative transfer. *Journal of Geophysical Research: Atmospheres*, *99*(D7), 14361-14371.

Light, T. E. L. (2020). A retrospective of findings from the FORTE satellite mission. *Journal of Geophysical Research: Atmospheres*, *125*(9), e2019JD032264.

Light, T. E., Suszcynsky, D. M., Kirkland, M. W., & Jacobson, A. R. (2001a). Simulations of lightning optical waveforms as seen through clouds by satellites. *Journal of Geophysical Research: Atmospheres*, *106*(D15), 17103-17114.

Light, T. E., Suszcynsky, D. M., & Jacobson, A. R. (2001b). Coincident radio frequency and optical emissions from lightning, observed with the FORTE satellite. *Journal of Geophysical Research: Atmospheres*, *106*(D22), 28223-28231.

Light, T. E. L., & Jacobson, A. R. (2002). Characteristics of impulsive VHF lightning signals observed by the FORTE satellite. *Journal of Geophysical Research: Atmospheres*, *107*(D24), ACL-8.

Light, T. E. L., & Jacobson, A. R. (2002). Characteristics of impulsive VHF lightning signals observed by the FORTE satellite. *Journal of Geophysical Research: Atmospheres*, *107*(D24), ACL-8.

Luque, A., Gordillo-Vázquez, F. J., Li, D., Malagón-Romero, A., Pérez-Invernón, F. J., Schmalzried, A., ... & Østgaard, N. (2020). Modeling lightning observations from space-based platforms (CloudScat. jl 1.0). *Geoscientific Model Development*, *13*(11), 5549-5566.

Mach, D. M., Christian, H. J., Blakeslee, R. J., Boccippio, D. J., Goodman, S. J., & Boeck, W. L. (2007). Performance assessment of the optical transient detector and lightning imaging sensor. *Journal of Geophysical Research: Atmospheres*, *112*(D9).

Mackerras, D. (1973). Photoelectric observations of the light emitted by lightning flashes. *Journal of Atmospheric and Terrestrial Physics*, *35*(3), 521-535.

Massey, R. S., Knox, S. O., Franz, R. C., Holden, D. N., & Rhodes, C. T. (1998). Measurements of transionospheric radio propagation parameters using the FORTE satellite. *Radio Science*, *33*(6), 1739-1753.

Peterson, M. (2019). Using lightning flashes to image thunderclouds. *Journal of Geophysical Research: Atmospheres*, *124*(17-18), 10175-10185.

Peterson, M. (2020). Modeling the Transmission of Optical Lightning Signals Through Complex 3-D Cloud Scenes. *Journal of Geophysical Research: Atmospheres*, *125*(23), e2020JD033231.

Peterson, M. (2021a). Holes in optical lightning flashes: Identifying poorly transmissive clouds in lightning imager data. *Earth and Space Science*, *8*(2),

e2020EA001294.

Peterson, M. (2021b). Where are the most extraordinary lightning megaflashes in the Americas?. *Bulletin of the American Meteorological Society*, *102*(3), E660-E671.

Peterson, M. (2022). FORTE Optical / RF Coincidence Data, https://doi.org/10.7910/DVN/AXWRQS, Harvard Dataverse, DRAFT VERSION

Peterson, M., & Rudlosky, S. (2019). The time evolution of optical lightning flashes. *Journal of Geophysical Research: Atmospheres*, *124*(1), 333-349.

Peterson, M., & Stano, G. (2021). The Hazards Posed by Mesoscale Lightning Megaflashes. *Earth Interactions*, *25*(1), 46-56.

Peterson, M., & Kirkland, M. W. (2020). Revisiting the detection of optical lightning superbolts. *Journal of Geophysical Research: Atmospheres*, *125*(23), e2020JD033377.

Peterson, M., & Lay, E. (2020). GLM Observations of the Brightest Lightning in the Americas. *Journal of Geophysical Research: Atmospheres*, *125*(23), e2020JD033378.

Peterson, M., Rudlosky, S., & Deierling, W. (2017). The evolution and structure of extreme optical lightning flashes. *Journal of Geophysical Research: Atmospheres*, *122*(24), 13-370.

Peterson, M., Rudlosky, S., & Zhang, D. (2020). Changes to the appearance of optical lightning flashes observed from space according to thunderstorm organization and structure. *Journal of Geophysical Research: Atmospheres*, 125, e2019JD031087. https://doi.org/10.1029/2019JD031087

Peterson, M., Light, T. E. L., & Shao, X.-M. (2021). Combined optical and radio-frequency measurements of a lightning megaflash by the FORTE satellite. *Journal of Geophysical Research: Atmospheres*, 126, e2020JD034411. https://doi.org/10.1029/2020JD034411

Peterson, M. J., Lang, T. J., Logan, T., Kiong, C. W., Gijben, M., Holle, R., Kolmasova, I., Marisaldi, M., Montanya, J., Pawar, S. D., Zhang, D., Brunet, M., & Cerveny, R. S. (2022a). New WMO Certified Megaflash Lightning Extremes for Flash Distance (768 km) and Duration (17.01 seconds) Recorded from Space, *Bulletin of the American Meteorological Society* (published online ahead of print 2022). Retrieved Feb 10, 2022, from https://journals.ametsoc.org/view/journals/bams/aop/BAMS-D-21-0254.1/BAMS-D-21-0254.1.xml

Peterson, M., Light, T. E., & Mach, D. (2022b). The Illumination of Thunderclouds by Lightning: 1. The Extent and Altitude of Optical Lightning Sources. *Journal of Geophysical Research: Atmospheres*, *127*(1), e2021JD035579.

Peterson, M., Light, T. E., & Mach, D. (2022c). The Illumination of Thunderclouds by Lightning: 2. The Effect of GLM Instrument Threshold on Detection

and Clustering. *Earth and Space Science*, *9*(1), e2021EA001943.

Peterson, M., Light, T. E., & Mach, D. (2022d). The Illumination of Thunderclouds by Lightning: 3. Retrieving Optical Source Altitude. *Earth and Space Science*, *9*(1), e2021EA001944.

Peterson, M., & Mach, D. (2022e). The Illumination of Thunderclouds by Lightning: 4. Volumetric Thunderstorm Imagery. *Earth and Space Science*, *9*(1), e2021EA001945.

Roussel-Dupré, R. A., Jacobson, A. R., & Triplett, L. A. (2001). Analysis of FORTE data to extract ionospheric parameters. *Radio Science*, *36*(6), 1615-1630.

Rudlosky, S. D., Goodman, S. J., Virts, K. S., & Bruning, E. C. (2019). Initial geostationary lightning mapper observations. *Geophysical Research Letters*, *46*(2), 1097-1104.

Salanave, L. E. (1961). The optical spectrum of lightning. *Science*, *134*(3488), 1395-1399.

Salanave, L. E. (1964). The optical spectrum of lightning. In *Advances in Geophysics* (Vol. 10, pp. 83-98). Elsevier.

Shao, X.-M., and A. R. Jacobson, 2001: Polarization observations of broadband VHF signals by the FORTE satellite. *Radio Sci.*, **36** (6), 1573– 1589, doi:10.1029/2000RS002600

Suszcynsky, D. M., Kirkland, M. W., Jacobson, A. R., Franz, R. C., Knox, S. O., Guillen, J. L. L., & Green, J. L. (2000). FORTE observations of simultaneous VHF and optical emissions from lightning: Basic phenomenology. *Journal of Geophysical Research: Atmospheres*, *105*(D2), 2191-2201.

Suszcynsky, D. M., Light, T. E., Davis, S., Green, J. L., Guillen, J. L. L., & Myre, W. (2001). Coordinated observations of optical lightning from space using the FORTE photodiode detector and CCD imager. *Journal of Geophysical Research: Atmospheres*, *106*(D16), 17897-17906.

Thomson, L. W., & Krider, E. P. (1982). The effects of clouds on the light produced by lightning. *Journal of Atmospheric Sciences*, *39*(9), 2051-2065.

Turman, B. N. (1977). Detection of lightning superbolts. *Journal of Geophysical Research*, *82*(18), 2566-2568.

Zhang, D., & Cummins, K. L. (2020). Time evolution of satellite-based optical properties in lightning flashes, and its impact on GLM flash detection. *Journal of Geophysical Research: Atmospheres*, 125, e2019JD032024. https://doi.org/10.1029/2019JD032024

Table 1. Frequencies of PDD events matched to LLS groups, TATR events, and NLDN strokes in the full PDD record (1997-2010) and the RF record (1997-2003) by waveform type

PDD Event Quality	All PDD Events	Any Matched Event	Matched LLS Group	Matche
		All	Single	All
	Full PDD Record (1997-2010)			
All PDD Events	10,428,904	4,304,950	3,097,450	4,206,2
Particle Filter	10,021,090	4,098,154	2,989,071	4,013,9
Isolated Waveform	4,279,989	1,556,153	1,195,581	1,514,9
Contained Waveform	1,806,662	646,608	532,308	630,726
Simple Waveform	1,414,730	559,363	460,320	546,236
	RF Record (1997-2003)			
All PDD Events	3,539,606	1,483,125	1,109,053	1,392,0
Particle Filter	3,368,312	1,406,389	1,062,294	1,329,8
Isolated Waveform	1,504,423	556,666	442,680	520,089
Contained Waveform	614,284	227,337	190,824	212,921
Simple Waveform	486,957	195,941	164,354	184,026

Table 2. Statistics of PDD optical pulse attributes measured over the full FORTE mission

PDD Waveform Parameter	Mean	Median	Standard Deviation		
	All Valid	Contained Waveform	Simple Waveform	All Valid	Contained
PDD Events (1997-2010)					
Effective Event Width	706 µs	427 µs	424 µs	633 µs	410 µs
Effective Pulse Width	633 µs	413 µs	412 µs	581 µs	395 µs
10-10% Full Width	1091 µs	754 µs	754 µs	1080 µs	735 µs
50-50% Full Width	497 µs	362 µs	362 µs	450 µs	345 µs
90-90% Full Width	100 µs	95 µs	100 µs	90 µs	90 µs
10-50% Rise Time	191 µs	102 µs	103 µs	135 µs	75 µs
10-90% Rise Time	336 µs	197 µs	197 µs	270 µs	165 µs
10-100% Rise Time	373 µs	233 µs	236 µs	315 µs	210 µs
100-10% Fall Time	717 µs	521 µs	518 µs	675 µs	495 µs
90-10% Fall Time	655 µs	462 µs	457 µs	615 µs	435 µs
50-10% Fall Time	403 µs	290 µs	288 µs	360 µs	270 µs

Table 3. Statistics of PDD optical pulse attributes for waveforms matched to LLS groups or TATR events

PDD Waveform Parameter	Mean	Median	Standard Deviation		
	Any Match	Contained Waveform	Simple Waveform	Any Match	Cont
LLS Matches (1997-2010)					
Effective Event Width	763 µs	452 µs	447 µs	714 µs	433 µ

PDD Waveform Parameter	Mean	Median	Standard Deviation		
Effective Pulse Width	698 µs	435 µs	433 µs	664 µs	417 µ
10-10% Full Width	1216 µs	805 µs	801 µs	1260 µs	780 µ
50-50% Full Width	564 µs	380 µs	379 µs	510 µs	360 µ
90-90% Full Width	120 µs	105 µs	109 µs	105 µs	105 µ
10-50% Rise Time	216 µs	112 µs	113 µs	150 µs	90 µs
10-90% Rise Time	378 µs	210 µs	209 µs	315 µs	180 µ
10-100% Rise Time	423 µs	251 µs	252 µs	360 µs	225 µ
100-10% Fall Time	793 µs	554 µs	549 µs	780 µs	540 µ
90-10% Fall Time	718 µs	489 µs	483 µs	690 µs	465 µ
50-10% Fall Time	436 µs	312 µs	309 µs	405 µs	300 µ
TATR Matches (1997-2003)					
Effective Event Width	571 µs	415 µs	414 µs	517 µs	405 µ
Effective Pulse Width	514 µs	400 µs	401 µs	477 µs	389 µ
10-10% Full Width	876 µs	728 µs	732 µs	870 µs	720 µ
50-50% Full Width	413 µs	352 µs	354 µs	375 µs	330 µ
90-90% Full Width	94 µs	100 µs	105 µs	90 µs	90 µs
10-50% Rise Time	142 µs	95 µs	96 µs	90 µs	75 µs
10-90% Rise Time	255 µs	183 µs	183 µs	195 µs	150 µ
10-100% Rise Time	292 µs	222 µs	225 µs	240 µs	195 µ
100-10% Fall Time	584 µs	506 µs	507 µs	555 µs	495 µ
90-10% Fall Time	526 µs	446 µs	444 µs	495 µs	435 µ
50-10% Fall Time	321 µs	282 µs	283 µs	285 µs	270 µ

Table 4. Statistics of PDD optical pulse attributes for waveforms matched to NLDN strokes

PDD Waveform Parameter	Mean	Median	Standard Deviation		
	Any Match	Contained Waveform	Simple Waveform	Any Match	Conta
NLDN -CG Matches					
Effective Event Width	508 µs	405 µs	402 µs	442 µs	386 µs
Effective Pulse Width	482 µs	393 µs	392 µs	418 µs	373 µs
10-10% Full Width	834 µs	697 µs	697 µs	720 µs	675 µs
50-50% Full Width	419 µs	353 µs	352 µs	345 µs	330 µs
90-90% Full Width	93 µs	101 µs	105 µs	75 µs	90 µs
10-50% Rise Time	120 µs	82 µs	82 µs	75 µs	60 µs
10-90% Rise Time	241 µs	170 µs	167 µs	180 µs	150 µs
10-100% Rise Time	279 µs	212 µs	211 µs	225 µs	180 µs
100-10% Fall Time	554 µs	485 µs	486 µs	465 µs	465 µs
90-10% Fall Time	499 µs	426 µs	424 µs	420 µs	405 µs
50-10% Fall Time	295 µs	261 µs	263 µs	240 µs	240 µs
NLDN +CG Matches					
Effective Event Width	608 µs	492 µs	495 µs	569 µs	476 µs

PDD Waveform Parameter	Mean	Median	Standard Deviation		
Effective Pulse Width	574 µs	483 µs	486 µs	548 µs	467 µs
10-10% Full Width	971 µs	823 µs	828 µs	945 µs	810 µs
50-50% Full Width	493 µs	449 µs	455 µs	465 µs	435 µs
90-90% Full Width	112 µs	141 µs	147 µs	90 µs	135 µs
10-50% Rise Time	158 µs	118 µs	119 µs	120 µs	105 µs
10-90% Rise Time	309 µs	242 µs	242 µs	270 µs	225 µs
10-100% Rise Time	357 µs	304 µs	308 µs	330 µs	285 µs
100-10% Fall Time	614 µs	519 µs	521 µs	555 µs	510 µs
90-10% Fall Time	550 µs	440 µs	439 µs	495 µs	420 µs
50-10% Fall Time	320 µs	255 µs	254 µs	255 µs	240 µs

Table 5. PDD timing statistics and estimated scattering and physical delays for events matched to TATR events and NLDN CG strokes. Two possible values for the source pulse width are considered: the typical 200 µs value used in Suszcynsky et al. (2000) and the TATR effective event width.

Source Pulse Width	PDD Trigger Delay (µs)	Time of Flight (µs)	Correlation Time (µs)	P
	Mean	Median	Mean	M
PDD and TATR Matches				
Suszcynsky et al. (2000)	286	267	0	0
TATR Event Width				
PDD and NLDN -CG Matches				
Suszcynsky et al. (2000)	3400	3393	3093	30
TATR Event Width				
PDD and NLDN +CG Matches				
Suszcynsky et al. (2000)	3609	3585	3090	30
TATR Event Width				

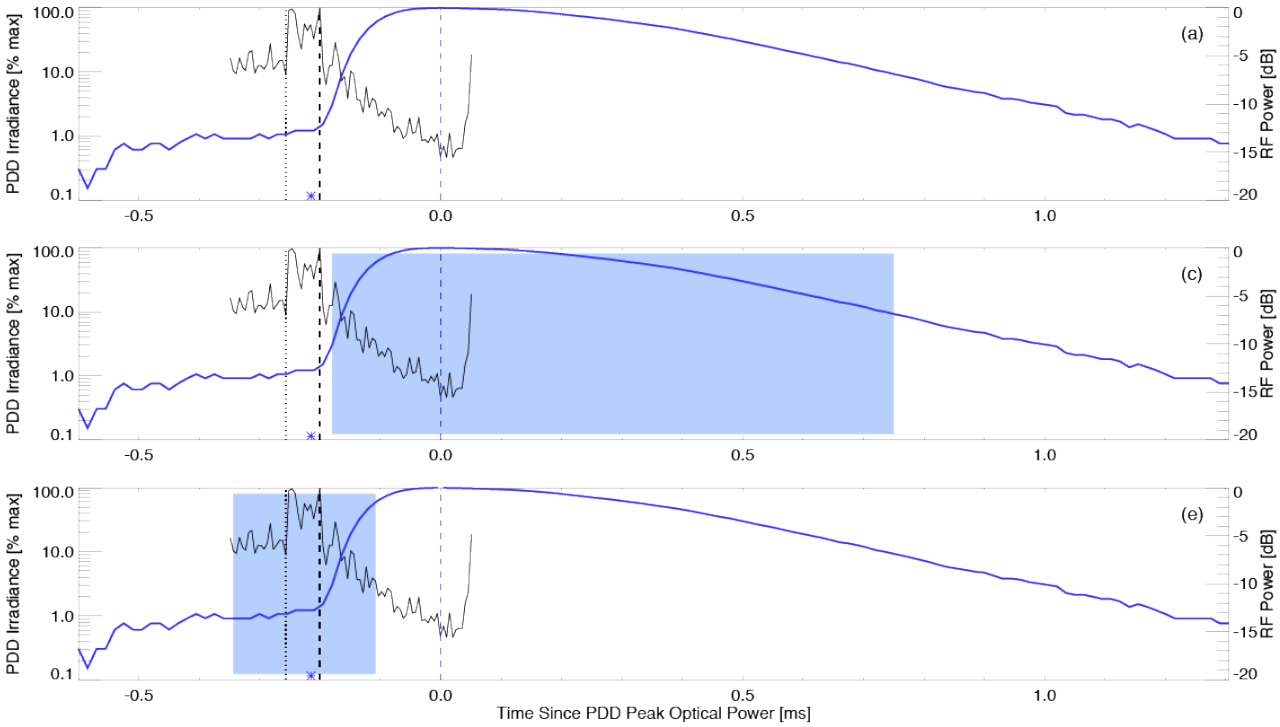
PDD Irradiance [% max]
100.0
10.0
1.0
0.1
RF Power [dB]
0
-5
-10
-15
-20
(a)
(c)
(e)
-0.5
0.0
0.5
1.0
Time Since PDD Peak Optical Power [ms]

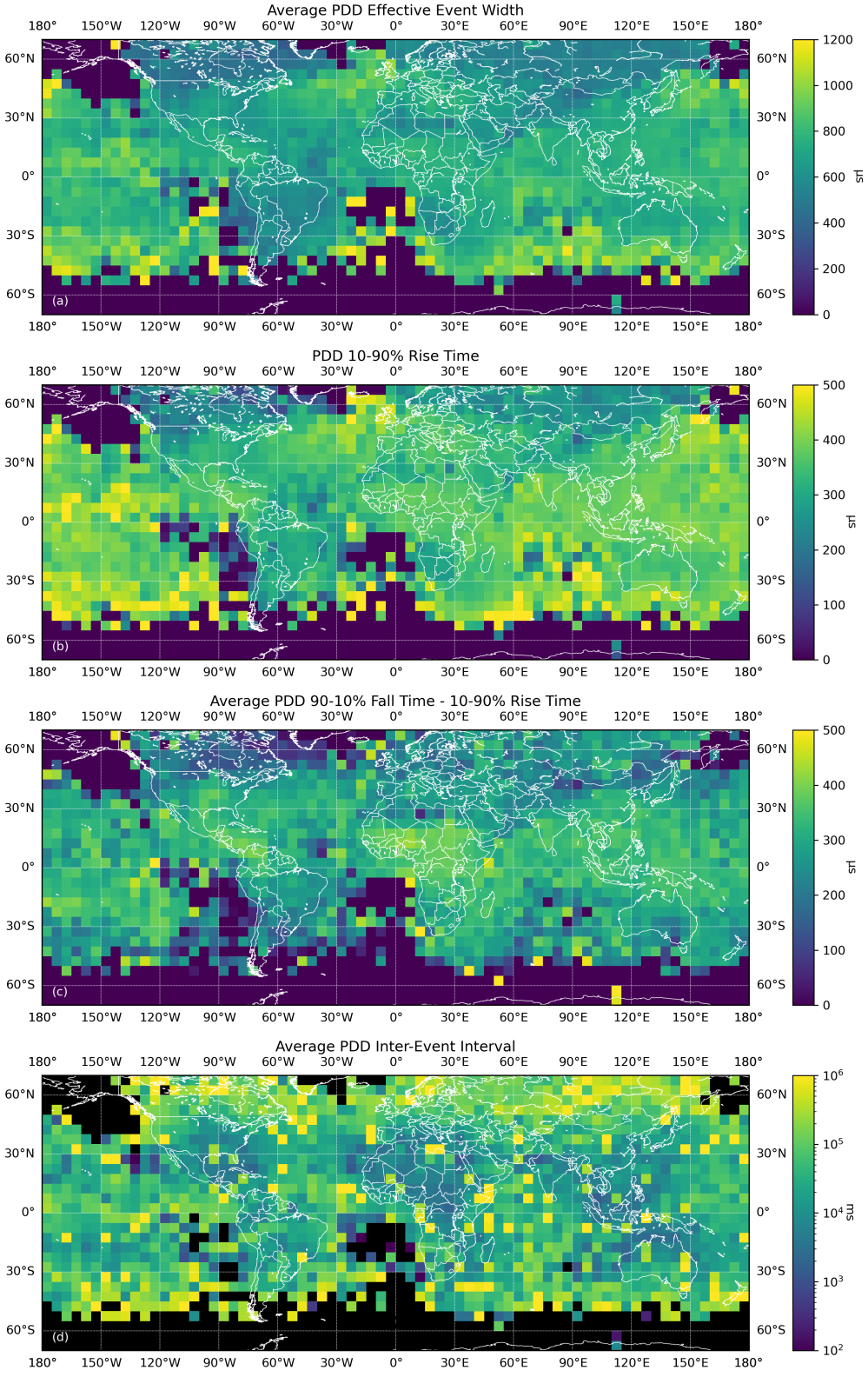
Average PDD Effective Event Width
PDD 10-90% Rise Time
Average PDD 90-10% Fall Time - 10-90% Rise Time
Average PDD Inter-Event Interval
180° 150°W 120°W 90°W 60°W 30°W 0° 30°E 60°E 90°E 120°E 150°E 180°
60°N
30°N
0°
30°S
60°S
(a)
(b)
(c)
(d)
1200
1000
800
600
400
200
0
500
300
100
10^6
10^5
10^4
10^3
10^2
srl
ms

Figure 2. Global distribution of the average effective event width (a), 10-90% rise time (b), 90-10% fall time – 10-90% rise time difference (c), and inter-event interval (d) for PDD events matched with another FORTE detection.

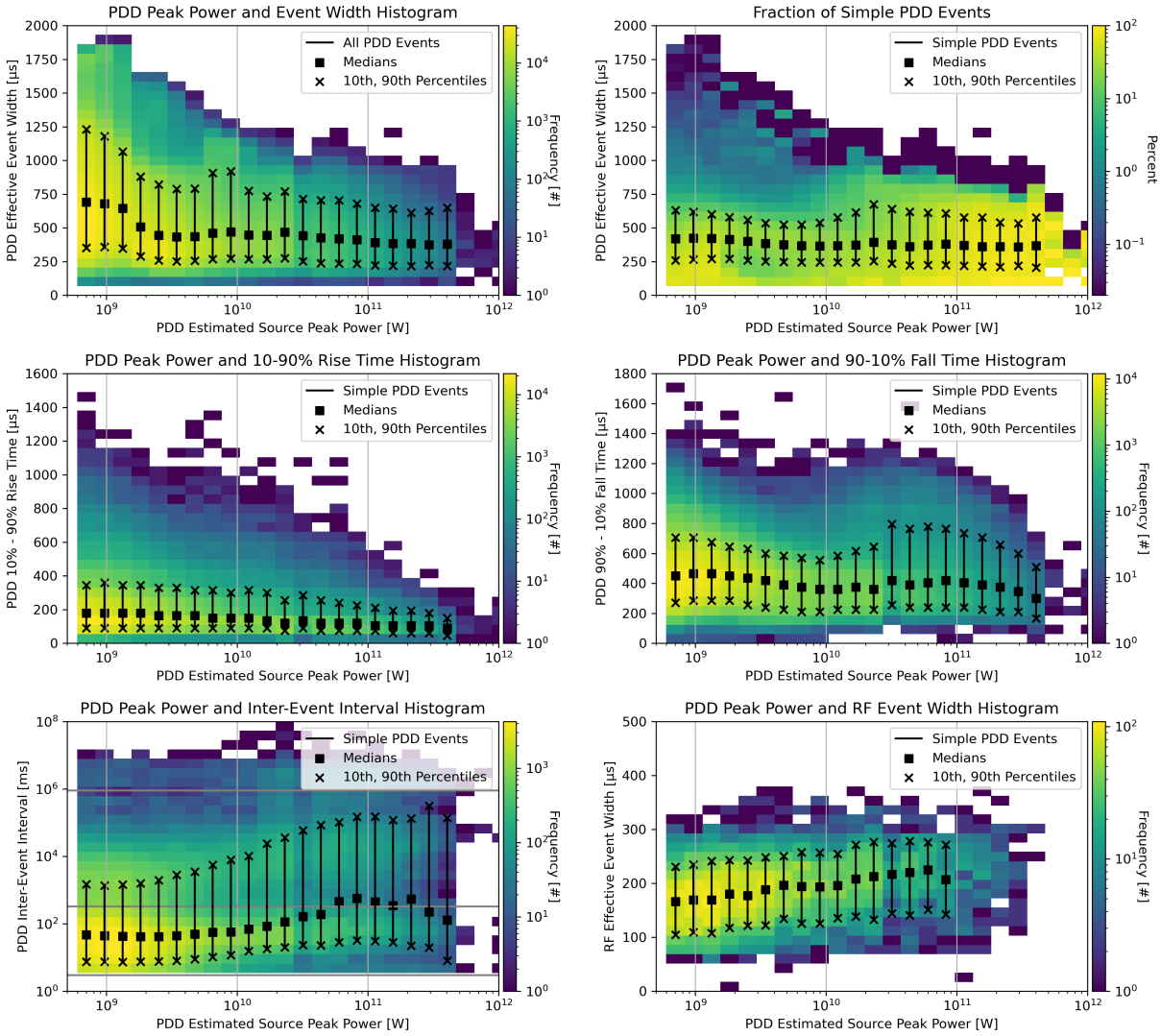

Figure 3. Two-dimensional histograms between PDD estimated source peak power and PDD effective event width (a,b), PDD 10-90% rise time (c), PDD 90-10% fall time – 10-90% rise time difference (d), PDD inter-event interval (e), and RF event width (f). Shading represents frequency in all panels except (b), which shows the fraction of simple PDD events at each point. The medians (square symbols) and 10^{th} and 90^{th} percentiles (x symbols) for the pulses in each peak optical power bin are overlaid.

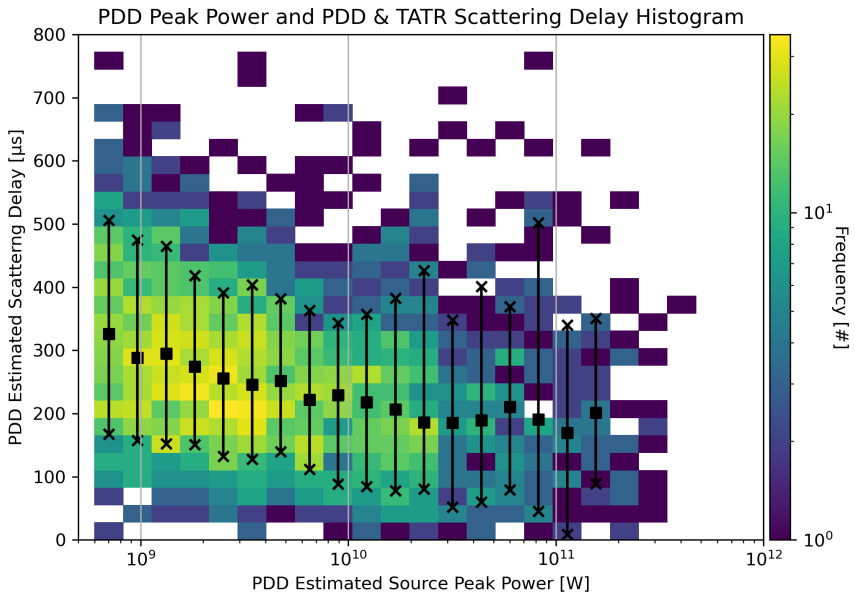

Figure 4. As in Figure 3, a two-dimensional histogram of PDD estimated source peak power and estimated scattering delay. Lines connect the median (square symbols) and 10^{th} and 90^{th} percentiles (x symbols) for the events in each peak power bin.

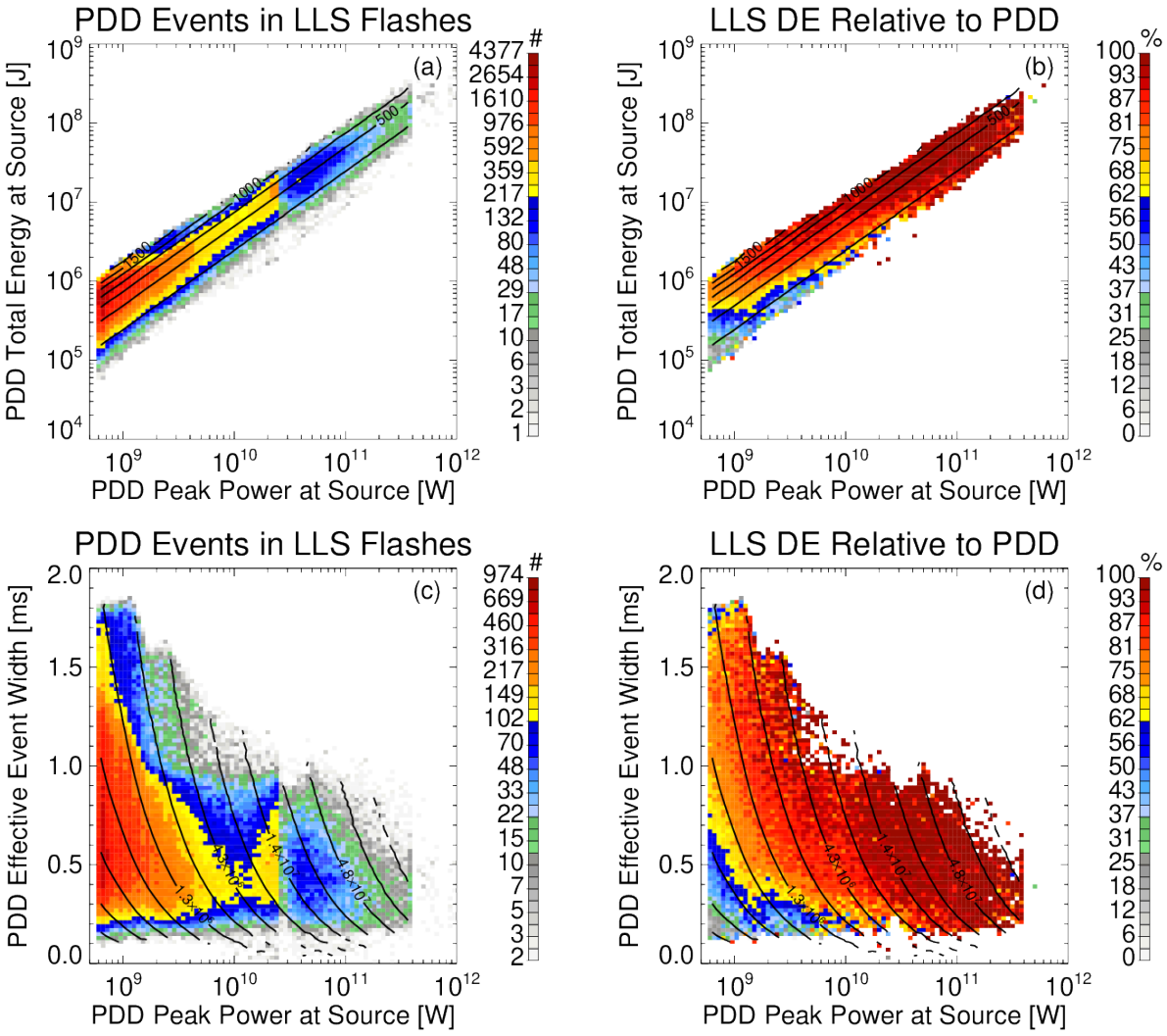

Figure 5. Two-dimensional histograms between PDD estimated peak power and either total energy at the source (a) or effective event width (c) for the PDD events that occur within LLS flashes and the corresponding Detecting Efficiencies (DE) of LLS relative to PDD at the event / group level (b,d). Line overlays depict the effective event widths associated with each combination of peak power and total energy (a,b) or the total energy associated with each combination of peak power and pulse width (c,d).

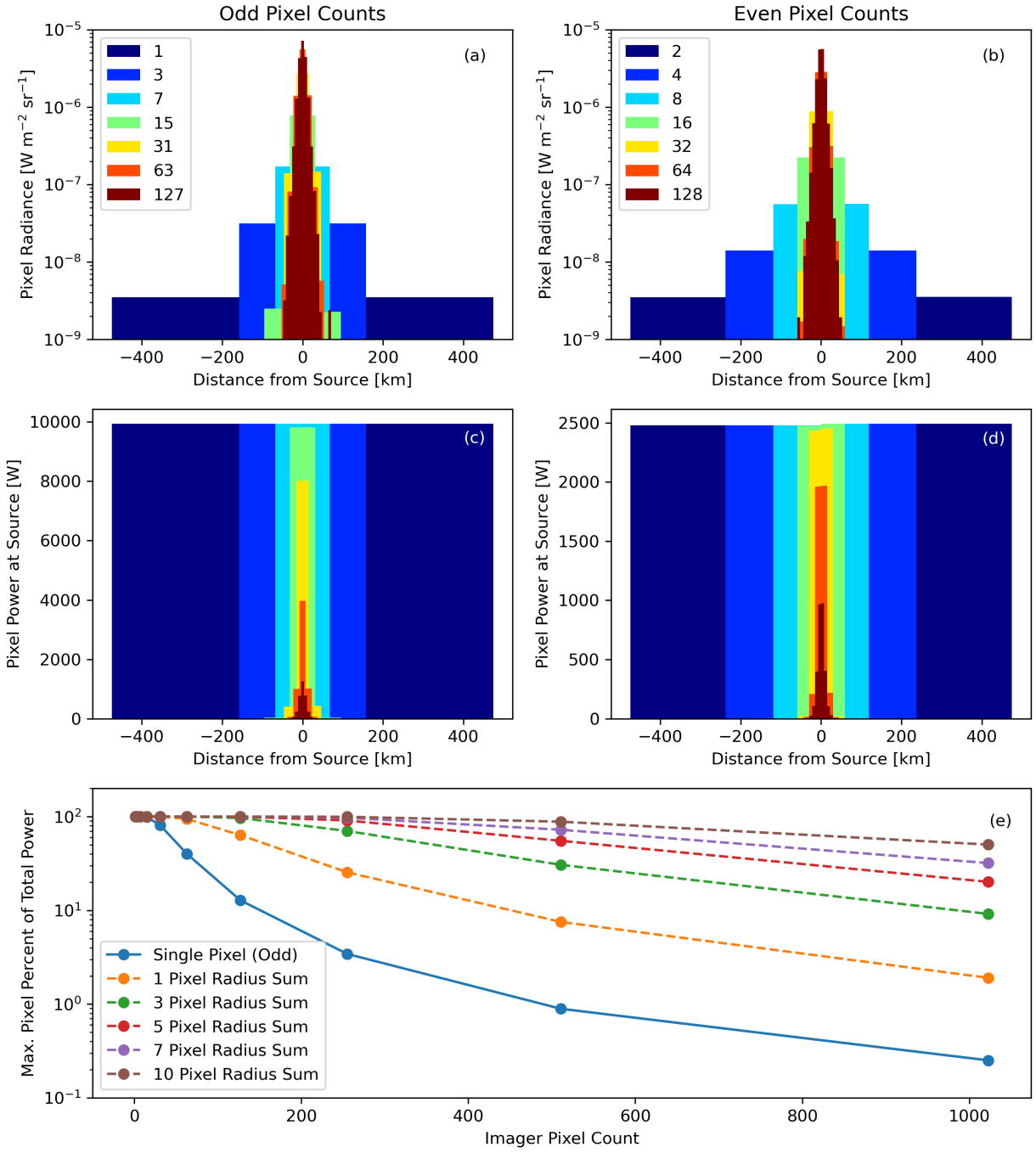

Figure 6. Radiance (a,b) and pixel power (c,d) cross sections through the

centers of optical pulses modeled with CloudScat where the emitter was located the base of a 14-km cloud and imaged from the FORTE altitude with imagers of varying pixel resolutions. Odd counts (a,c) have the source located at the center of a pixel, while even counts (b,d) have the source located at the boundaries between 4 pixels. Fractions of the total power in the brightest pixel at each resolution are shown in (e).

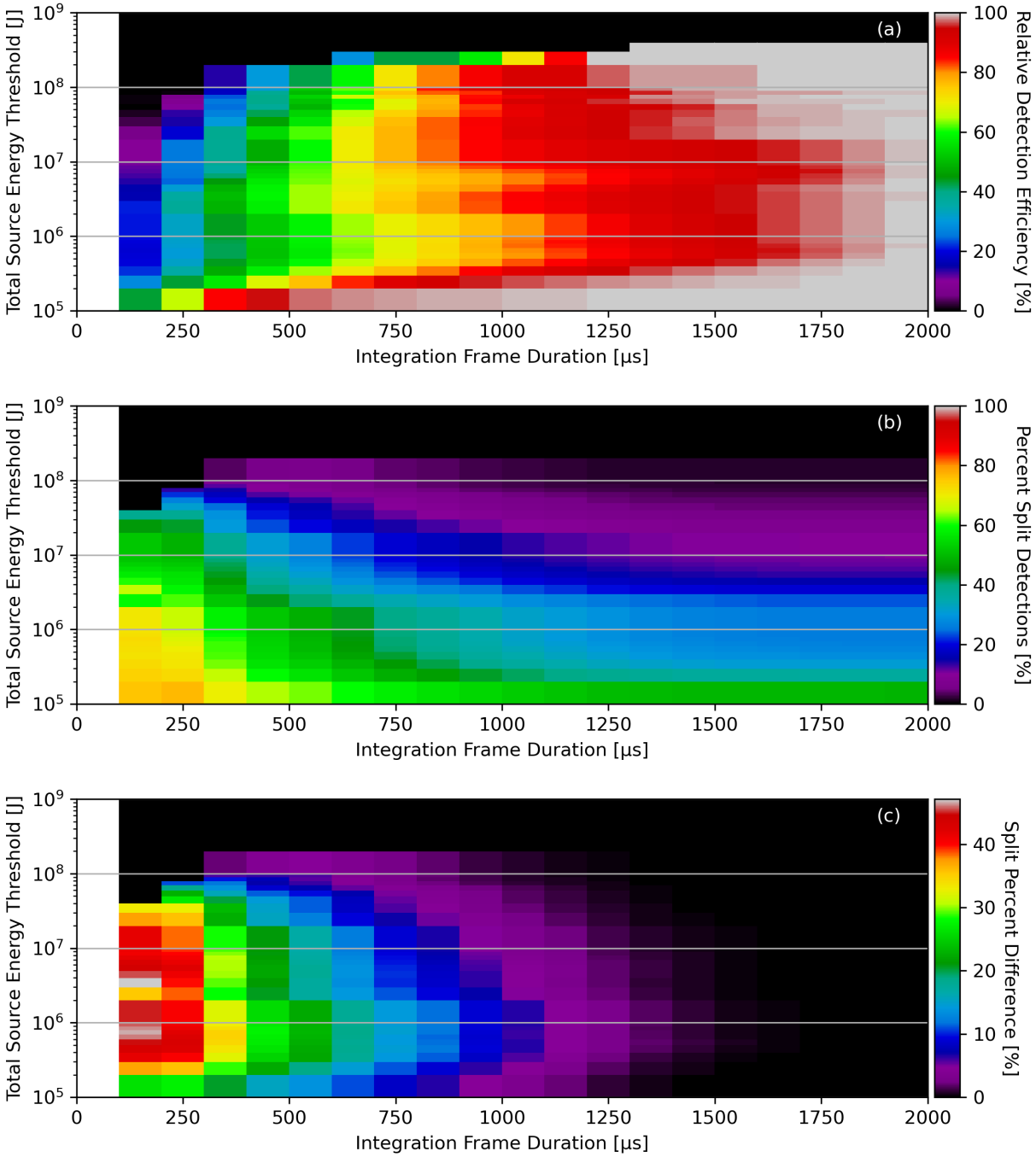

Figure 7. PDD-relative DEs (a), frequencies of split pulses (b), and split

pulse frequencies relative to a 2-ms integration frame for each combination of integration frame duration and total source energy threshold.